Journal of Power Sources 195 (2010) 6764–6773

Contents lists available at ScienceDirect

Journal of Power Sources

journal homepage: www.elsevier.com/locate/jpowsour

Transport, chemical and electrochemical processes in a planar solid oxide fuel cell: Detailed three-dimensional modeling

Thinh X. Ho [a,b,*], Pawel Kosinski [a], Alex C. Hoffmann [a], Arild Vik [b]

[a] Department of Physics and Technology, University of Bergen, Allegt 55, 5007 Bergen, Norway
[b] Prototech AS, Fantoftvegen 38, 5892 Bergen, Norway

ARTICLE INFO

Article history:
Received 30 September 2009
Received in revised form 27 March 2010
Accepted 30 March 2010
Available online 9 April 2010

Keywords:
SOFC
Composite electrode
Modeling
Three-dimensional
Simulation

ABSTRACT

A detailed numerical three-dimensional (3D) model for a planar solid oxide fuel cell (SOFC) is developed in this paper. The 3D model takes into account detailed processes including transport, chemical and electrochemical processes taking place in the cell. Moreover, effects of the composite electrodes are taken into account by considering an electrochemically active layer of finite thickness in each of the electrodes. The developed model is applied to a repeating unit of an anode-supported SOFC working under direct internal reforming conditions. Detailed results for chemical species, temperature, current density and electric potential distribution are presented and discussed. It was found that the temperature distribution across the cell is more uniform in the interconnects than in the inner part of the cell. However, only small differences in the electric potential between the electrode and the corresponding interconnect are found. The current density in the electrodes is found to be high near the electrolyte and low deep into the electrochemically active layer. The current density is also low under the ribs of the interconnects.

1. Introduction

The operation of solid oxide fuel cells (SOFCs) involve transport phenomena, chemical reactions and electrochemical processes in a multiphase system. These phenomena take place both in series and in parallel at high temperatures (500–1000°) in the complex and sophisticated structures of the main SOFC components, consisting of gas channels, porous electrodes and dense electrolyte and interconnects. In order to predict the performance of SOFCs, accurate modeling of the detailed processes is indispensably important.

One advantage of a numerical model is that it can provide detailed insights into the cells that cannot be gained by experiments. Additionally, it helps investigating the impacts of each process parameter and their interaction, giving information for cell optimization. Research aimed at modeling of SOFCs has been increasing rapidly during the last two decades, especially the last few years.

Regarding 3D numerical models, there have been several publications in the last few years [1–5]. Recknagle et al. [2] predicted the distribution of temperature and current density in a planar cell with different flow configurations. Nikooyeh et al. [3] investigated the thermal and electrochemical behavior of a repeating unit of an anode-supported cell with direct internal reforming of methane. Ohmic heat losses were not taken into account in the model. In the work of Zhang et al. [4], the distribution of current density and electric potential in the positive electrode–electrolyte–negative electrode (PEN) and the interconnects of half a repeating unit of SOFCs was analyzed using a Fluent-based model. Recently, Chaisantikulwat et al. [5] modeled the dynamic behavior of a unit planar cell as a consequence of step changes in the load current and input hydrogen concentration. It was found that the cell needs about 400 s to settle down after sudden changes of both current density and hydrogen concentration.

In the mentioned references, the electrochemical reactions and the associated heat were implemented either at the electrode–electrolyte interfaces [4,5] or in the whole 1000 μm thick anode [3] or even the whole PEN of 760 mm thickness [2]. Moreover, the output cell voltage was modeled as the Nernst potential minus ohmic, activation and concentration polarizations estimated from empirical relations. Concentration polarization was neglected in [3].

Numerical 1D and 2D models, in which the processes taking place in the composite electrodes are taken into account in a more detailed way can be found in [6–14]. Zhu et al. [6] used a quasi-2D model, in which the electrodes were discretized along their thickness and length, with implementation of heterogeneous chemistry and electrochemistry, though the later was implemented

Abbreviations: ADL, anode diffusion layer; ACL, anode catalyst layer; CDL, cathode diffusion layer; CCL, cathode catalyst layer.

* Corresponding author at: Department of Physics and Technology, University of Bergen, Allegt 55, 5007 Bergen, Norway. Tel: +47 55 57 41 28; fax: +47 55 57 41 14.
E-mail address: thinh.ho@ift.uib.no (T.X. Ho).

0378-7753/$ – see front matter © 2010 Elsevier B.V. All rights reserved.
doi:10.1016/j.jpowsour.2010.03.090

Nomenclature

A_{ac}	specific electrochemically active area (m^{-1})
c	constant-volume specific heat ($J\,kg^{-1}\,K^{-1}$)
C	effective concentration ($C\,m^{-3}$) or F ($mol\,m^{-3}$)
C_i	oxygen-ion concentration ($mol\,m^{-3}$)
D	diffusion coefficient ($m^2\,s^{-1}$)
e	specific internal energy ($J\,kg^{-1}$)
E_{cell}	potential (V)
f	unit conversion constant
F	Faraday constant (96,487 $C\,mol^{-1}$)
$F_{h,j}$	diffusive energy flux component ($J\,m^{-2}\,s^{-1}$)
ΔH	enthalpy of reaction ($J\,mol^{-1}$)
i	current density ($C\,m^{-2}\,s^{-1}$)
i_0	exchange current density ($C\,m^{-2}\,s^{-1}$)
j	transfer current ($C\,m^{-3}\,s^{-1}$)
k	thermal conductivity ($W\,m^{-1}\,K^{-1}$)
K	permeability of porous media ($kg\,m^{-3}\,s^{-1}$)
p	pressure (Pa)
Q_c	chemical heat source ($J\,m^{-3}\,s^{-1}$)
Q_e	electrochemical heat source ($J\,m^{-3}\,s^{-1}$)
Q_{Ohm}	ohmic heat source ($J\,m^{-3}\,s^{-1}$)
$\bar{r}$	pore radius (m)
R	universal constant of gas (8.314 $J\,mol^{-1}\,K^{-1}$)
R_{ref}	reforming reaction rate ($mol\,m^{-3}\,s^{-1}$)
R_{sh}	shift reaction rate ($mol\,m^{-3}\,s^{-1}$)
R_e	overall cell reaction rate ($mol\,m^{-3}\,s^{-1}$)
s_i	charge source term ($C\,m^{-3}\,s^{-1}$)
T	temperature (K)
u_i	velocity component ($m\,s^{-1}$)
x_i	Cartesian coordinate (m)

Greek letters

η	activation overpotential (V)
ϵ	porosity
λ	ionic conductivity ($\Omega^{-1}\,m^{-1}$)
Φ	potential (V)
ρ	gas mixture density ($kg\,m^{-3}$)
τ	tortuosity
τ_{ij}	stress tensor (Pa)

Subscripts

a	anode catalyst/active layer
c	cathode catalyst/active layer
e	electronic phase/electrolyte
i	ionic phase
i, j, k	Cartesian directions

only at the electrode–electrolyte interfaces. Results for chemical species concentration were obtained. A limitation of the model is that constant temperature was assumed throughout the cell. The model was later improved by removing the isothermal assumption [7]. In the work of Zhu and Kee [8], chemistry and charge transport taking place in the PEN of a planar SOFC were analyzed using a 1D approach. Current density and electric potential distributions across the PEN were obtained. Additionally, the effect of particle sizes in a 50 μm thick functional layer in the anode close to the electrolyte were investigated. It was found that smaller particles generally improve the cell performance as results of an increased three-phase boundary length. Similar results were also found by Nam and Jeon [9] for SOFCs at intermediate temperatures (600–800°C) using an isothermal micro-model, in which only the PEN was considered. Hussain et al. [10] adopted an electrochemical reaction zone of 20 μm thickness both in the anode and cathode

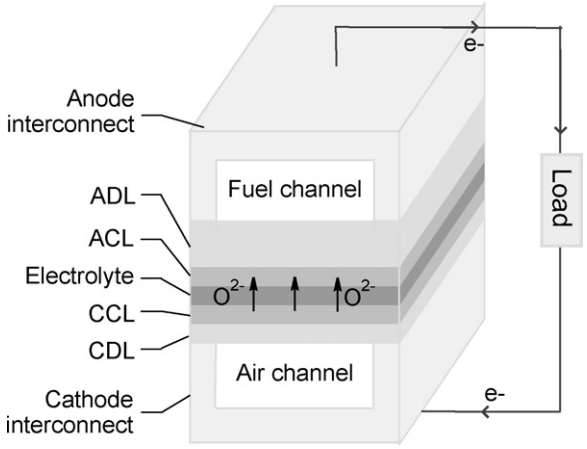

Fig. 1. Schematic diagram of a repeating unit anode-supported cell.

in their isothermal model. The model was 1D and only variations across the cell thickness were observed. In the work of Kenney and Karan [13], who studied the performance of a composite cathode of a planar SOFC using a 2D across-the-channel model, the thickness of the functional layer, i.e. the electrochemical reaction zone, in the cathode was varied in the range of 5–30 μm. It was found that addition of a current collector layer covering the functional layer results in an increase in the average current density because the current is higher underneath the interconnect.

In addition to those recently mentioned publications, we have developed a 2D model applied to different geometries and gas-flow configurations [15–17], in which the detailed processes happening in the porous electrodes including an electrochemically active layer of finite thickness were taken into account. In this paper we improve the model up to 3D while keeping its detail. Moreover, interconnects are included extending the modeling domain to the whole cell unit instead only part of it. Fig. 1 shows a schematic diagram of the cell unit used for the current work. This makes possible the modeling of a complete planar cell by repeating this unit. Hereinafter we will refer to this cell unit as the "cell".

We note that composite electrodes cannot be modeled as thin reactive boundaries since this does not capture the local current densities over the thickness. In our model, the electrodes are divided into two layers of which the layer adjacent to the electrolyte accommodates the electrochemical reactions and is called the catalyst (or electrochemically active) layer. The other layer of the electrodes was called "current collector" in our previous papers [16,15]. However, since this term is often used in fuel cell literature for interconnects, which are included in this 3D model, in order to avoid any possible confusion, we use the term "diffusion layer" for this. In Fig. 1 the abbreviations ADL and CDL denote the anode and cathode diffusion layers, respectively, and ACL and CCL denote the anode and cathode catalyst layers, respectively.

2. Electrochemical reactions

The modeling equations for the electrochemical reactions in the 3D cell are the same as in references [15,16] so that only a short account is given here.

The kinetics of the electrochemical reactions at the electrodes are calculated using a linearized version of the Butler–Volmer equation:

$$j = A_{ac} i_0 \left\{ \exp\left(\beta \frac{nF\eta}{RT}\right) - \exp\left[-\left(1-\beta\right)\frac{nF\eta}{RT}\right]\right\} \quad (1)$$

where j is the transfer current per unit volume of the catalyst layers, η is the activation overpotential, A_{ac} is the specific electrochemi-

cally active area in the catalyst layers, i_0 is the exchange current density, $\beta = 0.5$ is the symmetry coefficient, $n = 2$ is the number of participating electrons involved in the electrochemical processes and F is Faraday's constant.

For the case of low activation overpotentials, Eq. (1) can be linearized to give:

$$r = \frac{|j|}{F} = k_0|\eta| \tag{2}$$

where r is the electrode reaction rate based on molar change of electrons (mol m^{-3} s^{-1}) and k_0 is defined as $k_0 = 2A_{ac}i_0/RT$, a rate coefficient.

2.1. Cell voltage

Output voltage of the cell can be calculated as the electric potential difference between the cathode and anode interconnects:

$$E_{cell} = \Phi_{e,Cint} - \Phi_{e,Aint} \tag{3}$$

where E_{cell} is the output cell voltage and $\Phi_{e,Cint}$ and $\Phi_{e,Aint}$ are the electric potential of the cathode and anode interconnects, respectively.

In our previous works, it was given by the potential difference between the cathode and anode [15–17]. This would not result in any big errors since it was found that the electric potential difference between interconnects and electrodes is very small, i.e. 2.35 mV on the cathode side and 7.3 mV on the anode side [4].

The outer-most surfaces of the interconnects are assumed to possess uniform potentials fixed at 0.8 V on the cathode side and 0.1 V on the anode side.

2.2. Transport of charge

Transport of oxygen ions in the ionic phase of the electrolyte and the electrochemically active layers can be described using the Nernst–Planck equation [18,19]:

$$i = -DzF\left(\frac{\partial C_i}{\partial x} + zC_i\frac{F}{RT}\frac{\partial \Phi_i}{\partial x}\right) \tag{4}$$

where i is the current density due to the flow of oxygen ions, C_i is the oxygen-ion concentration, $z = 2$ is its valence and Φ_i is the electric potential of the ionic phase. Note that i is defined as the current flux (or superficial current density) normal to the electrolyte surface. The first term in the right-hand side of Eq. (4) represents the contribution due to concentration gradient of oxygen ions (diffusion), while the second term represents the contribution due to electric potential gradient.

The diffusion term of Eq. (4) is assumed to be negligibly small compared to the field-driven term as concentration of oxygen ions is high and almost uniform in YSZ material applied to SOFCs. The transport of oxygen ions then becomes ohmic and can be written as [15,16]

$$i = D\frac{\partial}{\partial x}\left(-C_i\frac{z^2F^2}{RT}\Phi_i\right) = D\frac{\partial C}{\partial x} \tag{5}$$

where $C = -C_i(z^2F^2/RT)\Phi_i$ is an "effective concentration" representing the ionic potential in the electrolyte and the ionic phases in the electrodes.

The last equation has the form of Fickian diffusion, an algorithm for which is built into Star-CD. Therefore, we use this algorithm to model the transport of ions in which D functions as an "effective diffusion coefficient" and takes on the value of $\lambda/96{,}487$ in case C is in C m^{-3} [15,16]. The ionic conductivity of the 8YSZ electrolyte, λ, is given as a function of temperature [20]:

$$\lambda = 85{,}000 \times \exp\left(-\frac{11{,}000}{T}\right), \tag{6}$$

thus making also D a function of temperature. Since we lack values for the ionic/electronic phase ratio, particle diameters, etc. for the composite electrodes we set their ionic conductivities to 0.35 of that of the electrolyte, which is in the high range of the predictions of the theory used by, among others, Zhu and Kee [8]. This value for the ionic conductivity in the anode should be validated in the future, since it implies that the tortuosity factor of the 8YSZ phase is almost unity, which is too high in light of recent knowledge from FIB-SEM measurements [21]. Moreover, the anode polarization is quite sensitive to its ionic conductivity.

Conservation of oxygen ions (charge) in the CCL–electrolyte–ACL assembly can be described as

$$\nabla \cdot i = s_i \tag{7}$$

where s_i is the charge source term, which takes on the value of r_cF in the CCL, $-r_aF$ in the ACL and zero in the electrolyte. r_c and r_c are the rates of the cathode and anode half-cell reactions, respectively, based on the molar change of electrons. A negative source term is used in the ACL corresponding to oxygen ions being consumed.

The ionic current density through the electrolyte, i_e, is equal to the electrochemical reaction rate in the whole catalyst layers at equilibrium:

$$i_e = F\int_{ACL} r_a\,dx = F\int_{CCL} r_c\,dx \tag{8}$$

where the integral is taken over the thickness of the anode and cathode catalyst layers (ACL and CCL), respectively.

Apart from the transport of oxygen ions, the transport of electrons in the electronic phase of the anode and cathode and the interconnects can also be modeled by the same algorithm. The assumption of zero (or close to zero) concentration gradients of electrons in the solid parts both on the anode and cathode sides is made. The transport is therefore ohmic due to the electric field. For calculation of the so-called "effective diffusion coefficient", the electric conductivity of the materials is used in the same way as described for the ionic conductivity above.

3. Modeling of chemical reactions

Reforming of methane to hydrogen in the high-temperature cell is taken into account in the model. The modeling equations for the reforming and shift reactions are the same as in references [15,16] and the equations are not repeated here.

The two reforming reactions are the methane steam reforming reaction and the water-gas shift reaction:

$$CH_4 + H_2O \rightleftharpoons CO + 3H_2 \tag{9}$$

$$CO + H_2O \rightleftharpoons CO_2 + H_2. \tag{10}$$

The methane steam reforming reaction is assumed to be catalyzed by nickel in the Ni–YSZ composite anode, and the kinetics are modeled as a single-step reaction (see also [22]). This reaction is assumed to take place mainly in the diffusional layer of the anode, but also in the electrochemically active layer. However, in the latter layer the kinetics are assumed to be much lower than in the former due to competition with the electrochemical reactions involving the much more mobile hydrogen.

Unlike the reforming reaction the water-gas shift reaction is non-catalyzed and therefore takes place throughout the fuel channel and the porous anode. The kinetics of this reaction are very fast, and the reaction is therefore assumed to always be in equilibrium at the high operating temperatures of the cell.

4. Modeling of mass and heat transport

In this section we use the Einstein summation convention with subscripts i and j denoting Cartesian coordinates. We only give the modeling equations for the transport of heat. The equations for transport of mass in the system are the same as in references [15,16], and we refer to the two references for the equations.

4.1. Transport of mass

Since, as stated above, the equations are given elsewhere we only give a rough account of the method here.

The flows of the total gaseous phases in the gas channels and the two electrodes are modeled by the standard balance equations for mass and momentum, the balance equation for mass augmented by a source term to account for the generation or consumption of mass in the electrochemical reactions.

In the porous parts of the domain, the momentum equation reduces to a form of the Darcy equation, $\nabla p = -K\,\mathbf{v}$ with K given by the Ergun equation for pressure drop through a porous medium.

Mass-balance equations are also solved for each of the chemical species separately, with diffusion in the porous layers taking into account Knudsen diffusion and the effect of the tortuosity of the pores.

4.2. Transport of heat

Energy conservation in the system can be given as follows:

$$\frac{\partial}{\partial t}(\epsilon\rho e) + \frac{\partial}{\partial x_j}\left(\rho u_j e + F_{h,j}\right) = \tau_{ij}\frac{\partial u_i}{\partial x_j} + Q_c + Q_e + Q_{\mathrm{Ohm}} \tag{11}$$

where $e = \bar{c}T - c_0 T_0$ is the specific internal energy, Q_c, Q_e and Q_{Ohm} are the heat source due to, respectively, the chemical reactions, the electrochemical reactions and resistance to flow of charges. $F_{h,j} = -k\partial T/\partial x_j$ is the diffusive thermal flux based on Fourier's law with k being the thermal conductivity of gas mixture and/or solid materials.

Radiation is not included in the model. Actually, Damm and Fedorov [23] showed that the radiation effects in planar SOFC electrodes are minimal and can safely be neglected. Moreover, Daun et al. [24] evaluated the importance of the radiative heat transfer in the electrode and electrolyte layers of a planar SOFC, using a 2D numerical approach. It was shown that it has only a negligible effect on the temperature field within these components, and does not need to be accommodated in comprehensive thermal models for planar SOFCs. In addition to those studies, Yakabe et al. [1] found that radiative heat transfer in the fuel and air channels of a planar SOFC has only a minor effect on the overall temperature distribution within the cell, relative to other modes of heat transfer. The inclusion of radiation calculations would have increased the computational time up to ten times and was not deemed worth it.

The heat source due to the chemical reactions can be determined as

$$Q_c = -R_{\mathrm{ref}}\,\Delta H_{\mathrm{ref}} - R_{\mathrm{sh}}\,\Delta H_{\mathrm{sh}} \tag{12}$$

where R_{ref} and R_{sh} are the rates of the reforming and shift reactions, respectively, based on the molar rates of change of CH_4 and CO, respectively, and ΔH_{ref} and ΔH_{sh} are the corresponding enthalpy changes. The reforming reaction is strongly endothermic ($\Delta H_{\mathrm{ref}} > 0$) while the shift reaction is slightly exothermic ($\Delta H_{\mathrm{sh}} < 0$). The chemical heat source is implemented throughout the fuel channel and the anode.

The heat source due to the electrochemical reactions can be evaluated via enthalpy changes and electrical work [25,26,22,3,27–32]:

$$Q_e = -R_e\,\Delta H_e - 2FR_eE_{\mathrm{cell}} \tag{13}$$

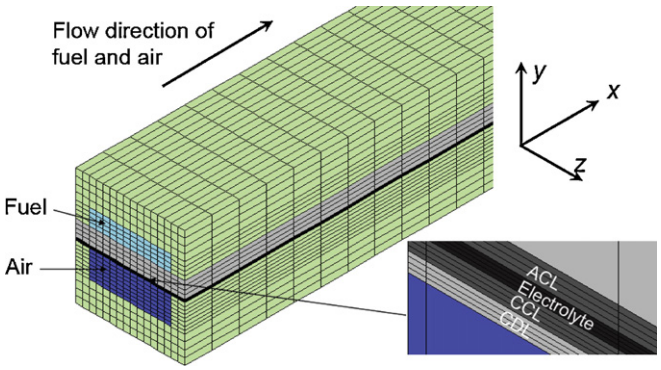

Fig. 2. Computational grid used for the current work.

where R_e is the reaction rate of the overall cell reaction based on the molar rate of change of H_2 and ΔH_e the corresponding enthalpy change. The electrochemical heat source is implemented in the anode catalyst layer of 30 μm thickness in this work. It was found in our previous paper [17], that the location of the electrochemical heat source, either in the ACL or the CCL, does not make any significant difference to the temperature field and the distribution of current density along the cell length. A similar conclusion was also drawn for a tubular SOFC by Fischer and Seume [33], who evaluated the heat source as entropy change implemented at the electrode–electrolyte interfaces.

The heat source due to resistance to flow of ions in the catalyst layers and the electrolyte, i.e. ohmic heat loss, can be determined as [11,5]

$$Q_{\mathrm{Ohm}} = \frac{i^2}{\lambda} \tag{14}$$

where i the local current density. However, since the electric conductivities of the Ni–YSZ composite anode, the LSM–YSZ composite cathode and interconnects of strontium-doped lanthanum chromite material are every large, the ohmic heat loss due to flow of electrons in the electrodes and interconnects is neglected.

5. Modeling implementation

Fig. 2 shows the computational grid, which consists of 64,000 elements. Referring to the coordinate system in Fig. 2 we will use the following terminology: "length" is in the x-direction, "thickness" is in the y-direction and "width" is in the z-direction.

A finite-volume-based grid is generated throughout the cell with 100 computational elements along the cell length and at least 4 in every cell component along its thickness. Four elements along the vertical or y-direction in the cell components are enough for the simulation to have convergent results. However, the air channel is divided vertically into 8 elements here, reducing the aspect ratio between elements in the air channel and the adjacent cathode diffusion layer, thus making the solution more stable and allowing the detailed velocity profile of the air in the channel to be observed. Grid convergence was ensured and this has been presented elsewhere [17]. Information about the grid and dimensions of each of the cell components is given in Table 1.

The interconnect-rib width is supposed to affect the cell performance since it conducts electrons between the interconnects and electrodes but impedes the gas flow in regions underneath it. Lin et al. [34] investigated effects of interconnect-rib size on concentration polarization of planar SOFCs using an analytical approach. Optimal rib design was related to a trade-off between the concentration polarization and electrical resistance, the resistance being mostly due to contact between the rib and electrode. For realistic electrical resistances, the rib width was suggested to be between

Table 1
Dimensions and grid information.

Parameters	Physical dimensions	No. mesh elements
Cell length	100 mm	100
Air channel thickness	1 mm	8
Fuel channel thickness	0.6 mm	4
ADL thickness	0.6 mm	4
ACL thickness	30 μm	4
CDL/CCL thickness	25 μm	4
Electrolyte thickness	20 μm	4
Interconnect thickness	1 mm	4
PEN width	4 mm	16
Air/fuel channel width	3 mm	12
Half interconnect-rib width	0.5 mm	2

Table 2
Physical properties of cell components.

Parameters	Values
Thermal conductivity, k ($W\,m^{-1}\,K^{-1}$)	
Anode/cathode/electrolyte	4/4/10
Interconnects	4
Ionic conductivity, λ ($\Omega^{-1}\,s^{-1}$)	
Electrolyte	$85,000 \times \exp\left(-11,000/T\right)$
ACL/CCL	$29,750 \times \exp\left(-11,000/T\right)$
Electronic conductivity, λ ($\Omega^{-1}\,s^{-1}$) [20]	
Anode	30,300
Cathode	12,800
Interconnects	3100
Anode/cathode porosity, ϵ	0.4/0.3
Anode/cathode tortuosity, τ	1.6/1.6
Anode/cathode pore diameter, $2\bar{r}$ (μm)	2/1
ACL density (Ni 50 wt.%, $kg\,m^{-3}$)	4300

1/3 and 2/3 of gas-channel width. Additionally, a value of 1/3 of the rib-to-channel width ratio was found to give the most realistic performance of a cathode by Kenney and Karan [13]. In our cell, the ratio is also given a value of 1/3. Half of the rib width is located on the either side of the gas channels.

Physical properties of the cell components are shown in Table 2. The anode channel is fed by a mixture of H_2O, CO_2, H_2, CH_4 and CO at 800 °C resulting from a preforming process of methane. The cathode is fed by air, also at 800 °C. The cell operates at a voltage of 0.7 V. Co-flow configuration is investigated. More details about the boundary and working conditions can be seen in Table 3.

6. Results and discussion

6.1. Chemical species

In this section, detailed distributions of chemical species concentration in the cell in all three dimensions are presented. Such profiles should be very useful for cell optimization and design, e.g.

Table 3
Boundary and operating conditions.

Parameters	Values and units
Fuel inlet	
Velocity	0.8 $m\,s^{-1}$
Temperature	1073 K
Fuel composition	H_2O 48.75%, H_2 26.86%, CH_4 17.07%, CO 2.40%, CO_2 4.91%
Air inlet	
Velocity	6.3 $m\,s^{-1}$
Temperature	1073 K
Air composition	O_2 21%, N_2 79%
Cell voltage	0.7 V

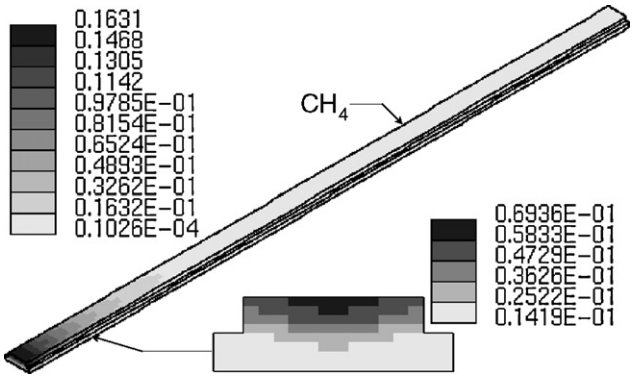

Fig. 3. Distribution of CH_4 concentration (%) in the fuel channel and the anode. The low figure is the cross-section at 10% of the cell length.

if regions depleted in fuel can be identified. Such regions are clearly visible in the results presented.

Results for the distribution of methane concentration in the fuel channel and the anode are presented in Fig. 3. As can be seen, the concentration of methane is rapidly reduced along the cell length due to the kinetically fast reforming reaction. The bottom plate in the figure shows that the concentration of CH_4 is lower in the anode than in the fuel channel, since most of the reforming takes place in the anode diffusion layer.

Fig. 4 presents the distribution of hydrogen concentration in the fuel channel and the anode. Hydrogen is produced by the reforming reaction making its concentration increase. However, further along the cell the content of hydrogen decreases due to the fact that the electrochemical reactions consume H_2 while almost all the methane has already reacted away in the region. More detailed information about the variations of H_2 concentration can be found in Fig. 5, in which three cross-sections at the positions of 10%, 50% and 90% of the cell length are shown. The concentration of H_2 in the anode, as compared to that in the fuel channel, can be seen to be higher at the first position (10% of the cell length) where the reforming reaction is dominant over the electrochemical reactions. However, at the other two positions it is lower as H_2 is consumed by the electrochemical reactions taking place in the anode catalyst layer.

The concentration of water is shown in Figs. 6 and 7. Initially low values in concentration of H_2O can be observed in Fig. 6 and in Fig. 7a, where a minimum value is seen in the anode diffusion layer. Downstream, H_2O is produced by the electrochemical reactions in the anode catalyst layer making its concentration rise, especially in the regions near the ACL as evident from Fig. 7b and c.

The distributions of concentration of CO and CO_2 are presented, respectively, in Figs. 8 and 9. As can be seen from Fig. 8, when

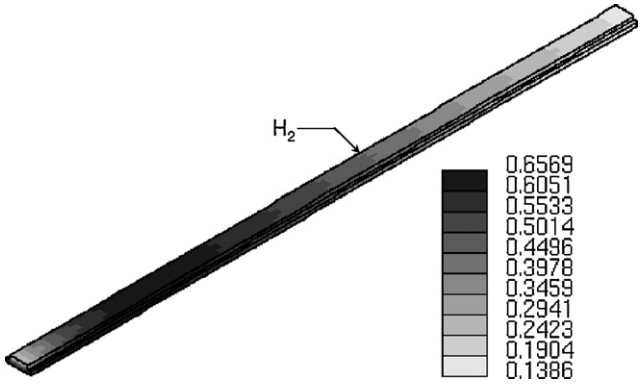

Fig. 4. Distribution of H_2 concentration (%) in the fuel channel and the anode.

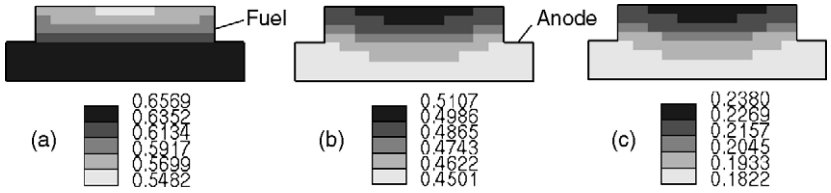

Fig. 5. Distribution of H_2 concentration (%) in cross-sections at 10% (a), 50% (b) and 90% (c) of the cell length.

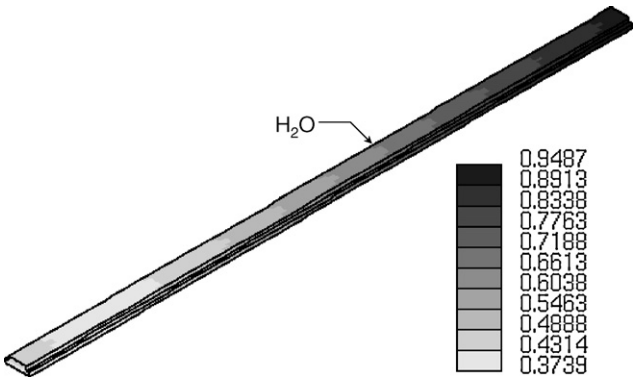

Fig. 6. Distribution of H_2O concentration (%) in the fuel channel and the anode.

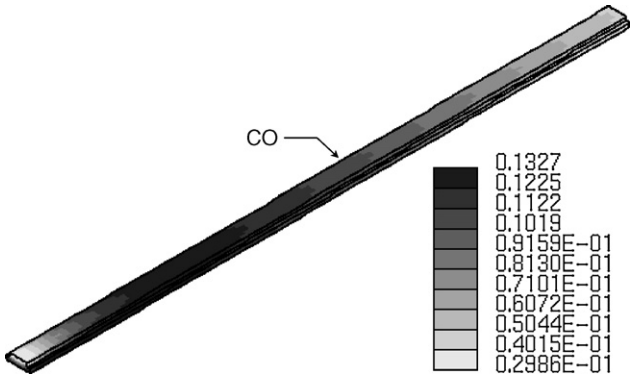

Fig. 8. Distribution of CO concentration (%) in the fuel channel and the anode.

entering the cell the content of CO increases due to the reforming reaction. However, further down the fuel stream it decreases due to the shift reaction, which proceeds in the direction of production of H_2 and CO_2. The increase of CO_2 along the cell length can be seen in Fig. 9.

Fuel utilization is as high as 76.2%, which is greater than 64.5% of the 2D model of otherwise similar conditions presented in [17] in which the interconnects were not included and only part of the PEN and the two gas channels were modeled. The difference can probably be due to extra contributions the electrochemical reactions by regions underneath the ribs. These regions are relatively large compared to the total electrochemical active regions, namely 25%.

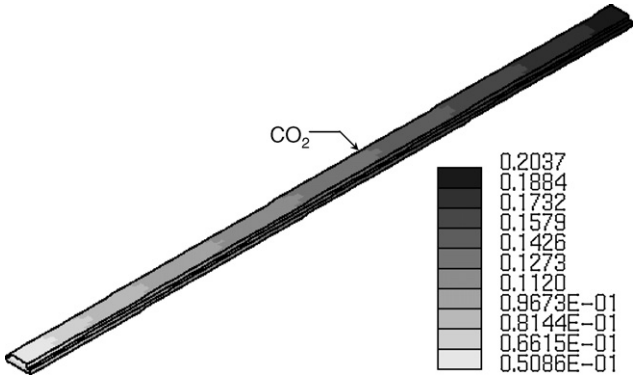

Fig. 9. Distribution of CO_2 concentration (%) in the fuel channel and the anode.

6.2. Temperature field

Results for the temperature field are presented in this section. Fig. 10 shows the distribution of temperature in the cell. Generally, the temperature increases along the cross-sectionally cell length. However, sub-cooling is found near the entrance of the cell as the minimum temperature (1036 K) drops significantly below the inlet temperature (1073 K). This is due to the endothermic reforming reaction, which proceeds rapidly as methane is present near the cell entrance.

Distributions of the temperature over the cell cross-section at 10%, 50% and 90% of the cell length are presented in Fig. 11. The temperature can be seen to distribute rather uniformly with maximum difference of less than 15 K. Extreme (low and/or high) temperatures manifest themselves in the gas channels, while in other regions the temperature distribution is more even. This is probably due to the fact that heat conduction in solid structures including the PEN and the interconnects is better than in the gas phase which flows laminarly.

The cross-sectional temperature distributions in the interconnects at the middle of the cell length is shown in Fig. 12. Compared to the temperature distribution in the inner part (Fig. 11b) with the maximum difference of around 14 K, the temperature is more uniform in the interconnects and the maximum difference of temperature is only about 5 K due to the relatively large thermal conductivity of the interconnects.

Cross-sectionally averaged temperature profiles in the air and fuel channels along the cell length are presented in Fig. 13 and compared with those obtained from our 2D model presented in [17]. The temperature profiles are very similar for the two models. However,

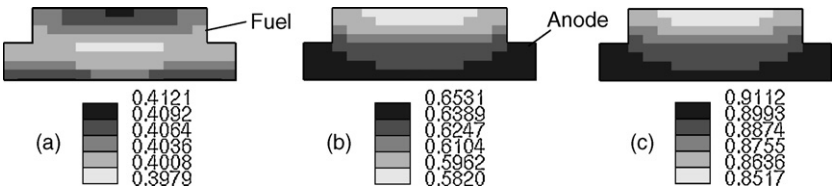

Fig. 7. Distribution of H_2O concentration (%) in cross-sections at 10% (a), 50% (b) and 90% (c) of the cell length.

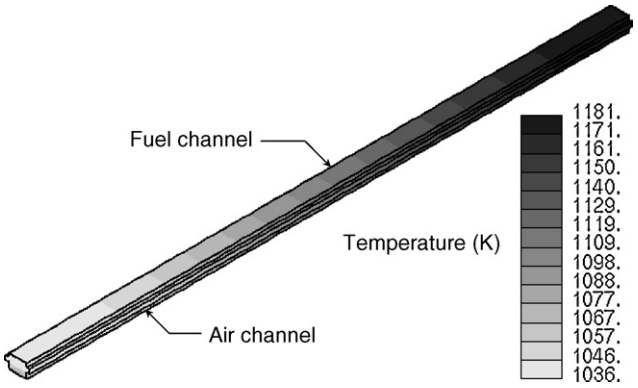

Fig. 10. Distribution of temperature in the cell. The interconnects are not shown.

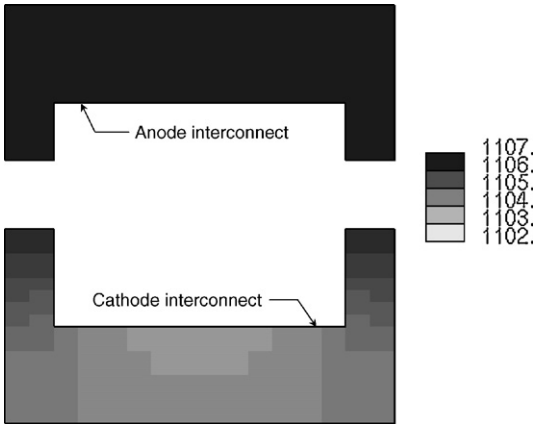

Fig. 12. Cross-sectional temperature distribution in the interconnects at the middle of the cell length.

the temperature difference between the profiles in the fuel and air channels is smaller for the 3D model than for the 2D model. Moreover, the profiles are flatter for the former than for the latter. This is probably due to the interconnects of high thermal conductivity making the temperature field more uniform. The averaged temperature profile in the electrolyte is very close to that in the fuel channel and is therefore not shown here.

6.3. Current density

Results for local current density in the anode catalyst layer (ACL) are presented in Fig. 14. Note that the current density is defined as the current flux normal to the electrolyte surface and generated locally by the electrochemical reactions. The integral of the reaction rate over the thickness of the ACL gives the current density in the electrolyte (see Eq. (8)). Moreover, the shown values are at the middle of the computational elements and not at the grid points. As can be seen, high values of the current density are observed near the electrolyte and low values of the current density near the anode diffusion layer. Moreover, low values of the current density are found at the two sides of the ACL, the regions underneath the interconnect-ribs. The latter is due to limitation of gas diffusion into and/or out of the regions, thus reducing the electrochemical kinetics. Very similar results of the current density in the cathode catalyst layer (CCL) are also obtained and ther efore not shown here.

The cross-sectionally averaged profile of the current density along the electrolyte is shown in Fig. 15 and compared with that obtained by the 2D model [17]. The difference between the two profiles is mainly near the exit of the cell where the fuel starts to deplete. As mentioned above, higher fuel utilization and hence more depletion of the fuel are obtained for the 3D case than for the 2D case. Therefore, the current density decreases faster after a peak for the former than for the latter. Furthermore, the average current density in the whole electrolyte is 0.516 A cm^{-2}, if the regions underneath the ribs are excluded it is about 0.563 A cm^{-2}, which is rather close the value of 0.589 A cm^{-2} obtained by the 2D model [17].

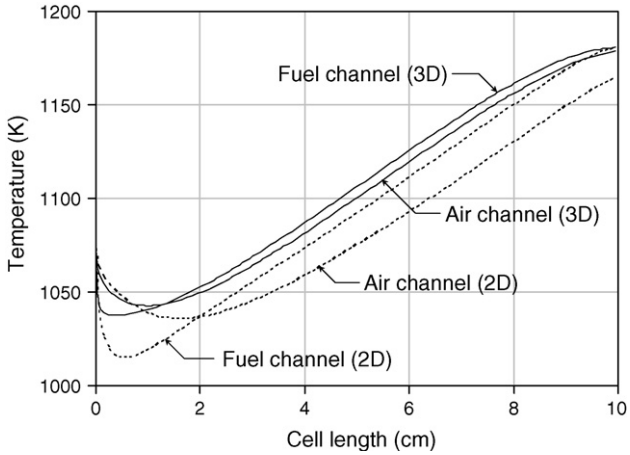

Fig. 13. Comparison of temperature profiles in the air and fuel channels between the current 3D model and the 2D model [17].

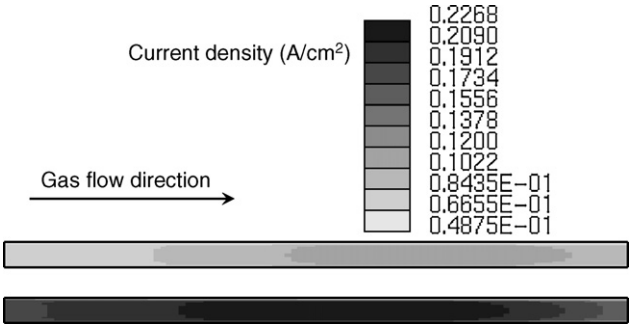

Fig. 14. Distribution of current density in the anode catalyst layer (ACL). Top figure: viewed from ADL–ACL interface; bottom figure: viewed from ACL–electrolyte interface.

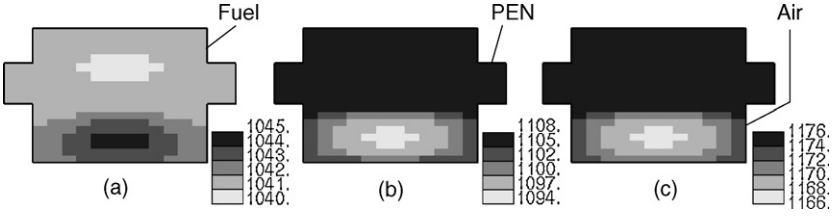

Fig. 11. Temperature field in cross-sections at 10% (a), 50% (b) and 90% (c) of the cell length.

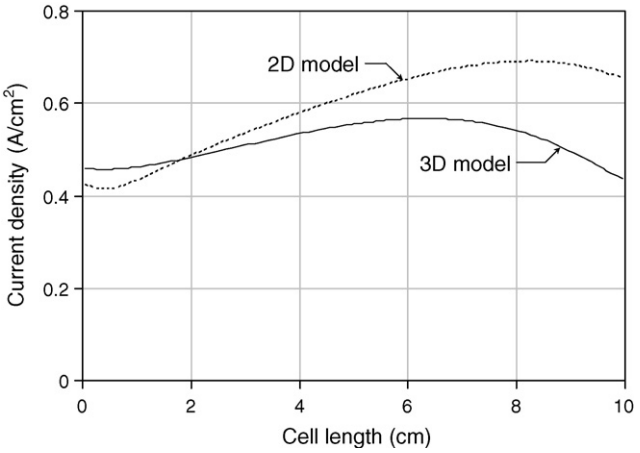

Fig. 15. Comparison of averaged current density profile along the cell length between the current 3D model and the 2D model [17].

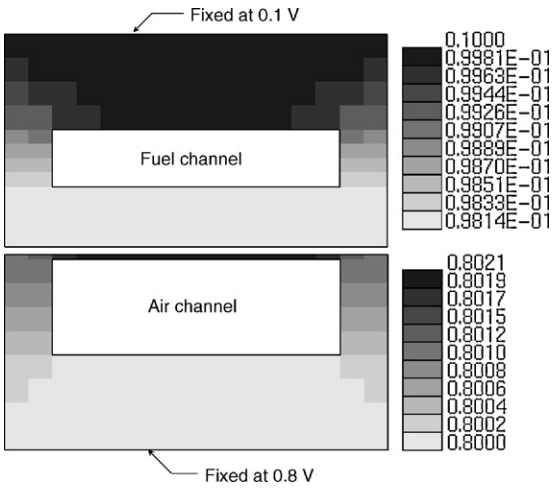

Fig. 17. Cross-sectional distribution of electric potential at the middle of the cell length.

6.4. Electric potential

In the current work, an electric potential of 0.1 V is applied to the top surface of the anode interconnect and 0.8 V to the bottom surface of the cathode interconnect. The electric potential fields in the cathode and cathode interconnect are shown in Fig. 16. The electric potential increases along the flow of electrons, i.e. high values of the potential in middle of the cathode catalyst layer corresponding to the high values of the current density.

The cross-sectional distribution of the electric potential at the middle of the cell length is presented in Fig. 17. On the anode side, the electric potential can be seen to be low in the anode catalyst layer and high near the top surface as electrons are being transported from the ACL to the anode interconnect. However, the potential differences are very small on both sides, i.e. around 2.1 mV on the cathode side and 1.9 mV on the anode side. In the work of Zhang et al. [4], the maximum potential difference between the interconnect and the electrode was found to be around 2.35 mV on the cathode side and 7.3 mV on the anode side of a planar electrolyte-supported SOFC.

A direct experimental validation of the present model is difficult at the present time, since experimental results for planar SOFCs in the literature, especially ones in which sufficient information about geometries, component materials and working conditions are given, are somewhat patchy. We can, however, at least roughly compare the results of the model with published results from simpler models. Nikooyeh et al. [3] studied the performance of a planar SOFC similar to ours, only their anode is slightly thicker (1000 μm compared to ours of 630 μm) and their electrolyte somewhat thinner (10 μm compared to ours of 20 μm). In order to compare the models, we adjusted the operating conditions of our cell to match those of Nikooyeh et al.: 0.7 V output voltage, 1073 K gas inlet temperatures, 75% fuel utilization and 8.5% of air-to-fuel ratio. To do this we had to "aim" for the conditions of Nikooyeh et al. by adjusting the air flow rate, since in our model the fuel utilization and hence the air-to-fuel ratio (which is 8 for Nikooyeh et al.) are not known in advance because the fuel consumption is temperature-dependent. Doing this we found trends of the chemical species concentration and temperature distributions along the cell length very similar to those presented by Nikooyeh et al. We found that the minimum and maximum temperatures in our cell were around 1026 K and 1127 K, respectively, very close to those of Nikooyeh et al. of 1023 K and 1120 K, respectively. The slight difference may be due to more ohmic heat being generated in our thicker electrolyte.

Trends are also similar to the results presented by Aguiar et al. [25], in which an anode-supported of similar cell components and at the same temperature inlet-conditions (1073 K) of the gas flows was investigated using a 1D numerical model. Both the anode and cathode of Aguiar et al. are thinner than ours while the cell length is much greater (40 cm compared to 10 cm in length) than ours. Moreover, the fuel used was richer in CH_4 resulting from 10% re-preforming of a mixture of CH_4 and H_2O (steam/carbon = 2). The maximum temperature at the exit of the cell and the minimum temperature near the cell entrance for the

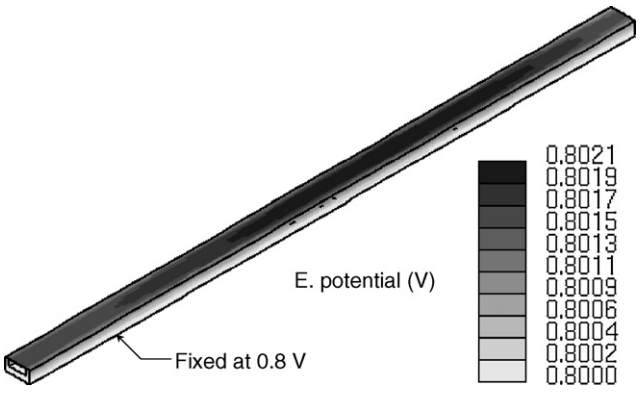

Fig. 16. Distribution of electric potential in the cathode and cathode interconnect.

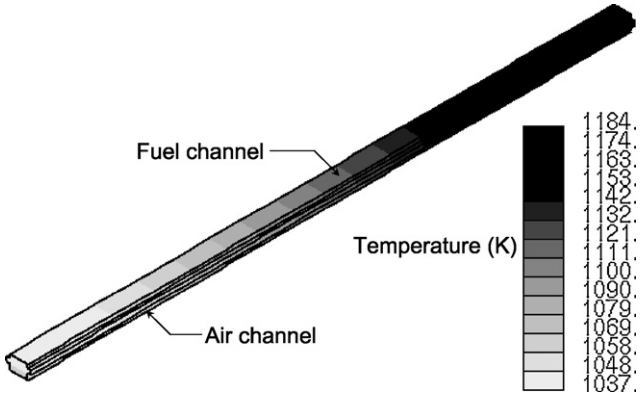

Fig. 18. Temperature distribution resulting from the fine grid.

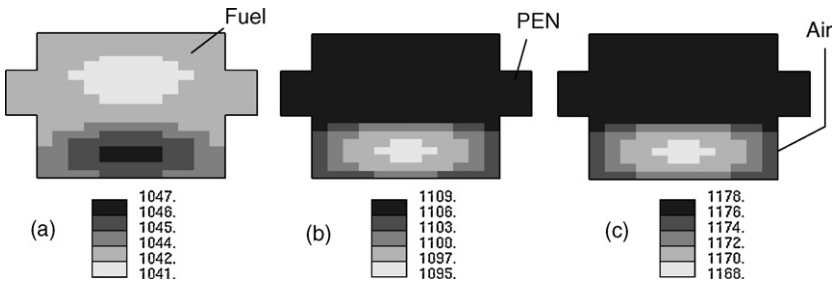

Fig. 19. Cross-sectional distribution of temperature at 10% (a), 50% (b) and 90% (c) of the cell length—the fine grid.

case of co-flow and 1073 K in inlet temperature were found to be somewhat smaller, namely 1150 K and 1005 K, respectively, than those in our cell, which were 1181 K and 1036 K, respectively. The probable reason is that more heat is consumed for the *in situ* reforming of CH_4 in the case of Aguiar et al. than in our case.

Moreover, our results of the electric potential distribution in the electrodes and interconnects are quite similar to those obtained by Zhang et al. [4] for a planar SOFC.

6.5. Grid independence

In this section we investigate the sensitivity of the results with respect to the grid size. One simulation was carried out using a finer grid. In the finer grid the number of computational elements is doubled in the anode, the fuel channel and the anode interconnect along the *y*-direction, i.e. normal to the electrolyte plane. In other subdomains of the cell the grid is kept the same compared to the grid used for the simulations presented above, i.e. the "base" grid. The reasons for refining the grid only on the anode side are that the chemical processes including the reforming and shift reactions take place on this side and we want to keep the computational effort at a moderate level. The fine grid consists of 89,600 elements (compared to 64,000 for the base grid).

The temperature distribution in the cell resulting from the fine grid is presented in Fig. 18. It can be seen that the temperature distribution is almost the same compared to the result presented in Fig. 10. The maximum temperature is slightly higher for the fine grid than for the base grid. However, the difference is only 3 K or about 0.25%. A close-up of the temperature distribution is shown in Fig. 19. Comparing this with the results from the base grid shown in Fig. 11, the temperature patterns are seen to be very similar, the differences being within 2 K, which are insignificant.

Moreover, results for the chemical species concentration and the current density in the electrolyte are almost the same for the two grids and thus not presented here. The sensitivity of the results to the fineness of the grid is therefore negligibly small.

Additionally, in another context we have studied grid independence of a two-dimensional problem, which has been presented elsewhere [17]. Two grids, which were different on the cathode side, were investigated. For the coarser grid, the cathode thickness was divided into 4 elements and the air channel also into 4 elements over its thickness. These numbers were doubled for the finer grid. However, the number of elements along the cell length was decreased to 100 in the latter grid instead of 200 for the former. In other parts of the cell the two grids are the same. Results of the temperature in the air and fuel channels for the two grids were compared, and they are redrawn in Fig. 20. As can be seen, the temperature is almost the same for the two grids. The grid used for the simulations presented in this paper is the same as the fine grid in the cathode and air channel. Therefore, increasing the number of elements along the cell length or refining the mesh on the cathode side would likely not give any important differences in the results.

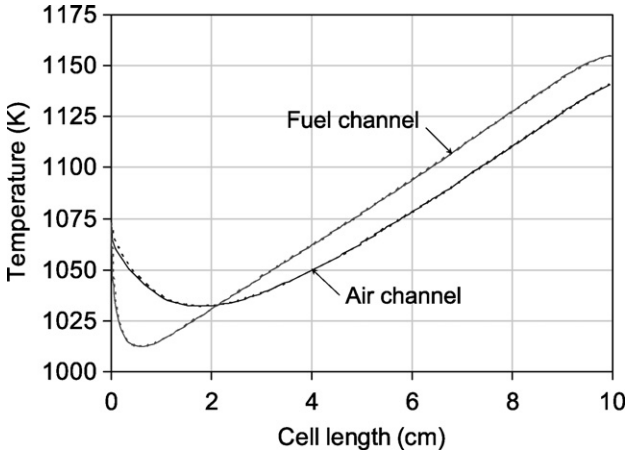

Fig. 20. Comparison of temperature in the air and fuel channels between the coarse (dashed-lines) and the fine (solid-lines) grids—the 2D model (redrawn from [17]).

7. Summary

A detailed numerical three-dimensional model was developed based on our two-dimensional model presented in [15–17]. The model took into account effects of the composite electrodes by considering an electrochemically active layer of finite thickness close to the electrolyte. Another important feature of the model is that the steady-state transport of charge was mimicked using an algorithm for Fickian diffusion built into the commercial computational package Star-CD. Moreover, the model used a single computational domain covering all the cell components including the gas channels, the PEN and the interconnects.

The developed 3D model was employed to investigate the transport and chemical and electrochemical processes taking place in a repeating unit of a planar anode-supported SOFC working under conditions of direct internal reforming. Detailed results for distributions of chemical species, temperature, current density and electric potential in the cell were shown and discussed. It was found that the temperature distribution across the cell is more uniform in the interconnects than in the inner part of the cell. Moreover, low values of the current density were observed in the regions underneath the interconnect-ribs due to limitation of gas diffusion caused by the presence of the ribs. Small differences in the electric potential between the electrode and the corresponding interconnect were observed due to the high electric conductivity of these materials.

The model is three-dimensional allowing variations in all three directions to be observed, while micro-processes occurring within the cell, contrary to other 3D models in the literature, are considered. This type of model can, after further validation, be an invaluable numerical tool for predicting cell performances and optimizing cell design.

Acknowledgment

Financial support from the NFR through the MSOFC program is gratefully acknowledged.

References

[1] H. Yakabe, T. Ogiwara, M. Hishinuma, I. Yasuda, J. Power Sources 102 (2001) 144–154.
[2] K.P. Recknagle, R.E. Williford, L.A. Chick, D.R. Rector, M.A. Khaleel, J. Power Sources 113 (2003) 109–114.
[3] K. Nikooyeh, A.A. Jeje, J.A. Hill, J. Power Sources 171 (2) (2007) 601–609.
[4] X. Zhang, G. Li, J. Li, Z. Feng, Energy Convers. Manage. 48 (3) (2007) 977–989.
[5] A. Chaisantikulwat, C. Diaz-Goano, E.S. Meadows, Comput. Chem. Eng. 32 (2008) 2365–2381.
[6] H. Zhu, R.J. Kee, V.M. Janardhanan, O. Deutschmann, D.G. Goodwin, J. Electrochem. Soc. 152 (2005) A2427–A2440.
[7] V.M. Janardhanan, O. Deutschmann, Chem. Eng. Sci. 62 (2007) 5473–5486.
[8] H. Zhu, R.J. Kee, J. Electrochem. Soc. 155 (7) (2008) B715–B729.
[9] J.H. Nam, D.H. Jeon, Electrochim. Acta 51 (17) (2006) 3446–3460.
[10] M.M. Hussain, X. Li, I. Dincer, J. Power Sources 161 (2) (2006) 1012–1022.
[11] L. Andreassi, G. Rubeo, S. Ubertini, P. Lunghi, R. Bove, Int. J. Hydrogen Energy 32 (17) (2007) 4559–4574.
[12] J.M. Klein, Y. Bultel, S. Georges, M. Pons, Chem. Eng. Sci. 62 (2007) 1636–1649.
[13] B. Kenney, K. Karan, Solid State Ionics 178 (3–4) (2007) 297–306.
[14] S.C. DeCaluwe, H. Zhu, R.J. Kee, G.S. Jackson, J. Electrochem. Soc. 155 (6) (2008) B538–B546.
[15] T.X. Ho, P. Kosinski, A.C. Hoffmann, A. Vik, Int. J. Hydrogen Energy 34 (2009) 3488–3499.
[16] T.X. Ho, P. Kosinski, A.C. Hoffmann, A. Vik, Chem. Eng. Sci. 64 (2009) 3000–3009.
[17] T.X. Ho, P. Kosinski, A.C. Hoffmann, A. Vik, Int. J. Hydrogen Energy (2010), doi:10.1016/j.ijhydene.2010.02.016.
[18] K. Krischer, in: R.C. Alkire, D.M. Kolb (Eds.), Advanced in Electrochemical Science and Engineering, Wiley-VCH Verlag GmbH & Co. KGaA, 2002.
[19] A.J. Bard, L.R. Faulkner (Eds.), Electrochemical Methods: Fundamentals and Applications, 2nd edition, Wiley, 2001, Chapter 1.
[20] U.G. Bossel, Facts & figures, an international energy agency SOFC task report, Berne, April 1992.
[21] H. Iwai, N. Shikazono, T. Matsui, H. Teshima, M. Kishimoto, R. Kishida, D. Hayashi, K. Matsuzaki, D. Kanno, M. Saito, H. Muroyama, K. Eguchi, N. Kasagi, H. Yoshida, J. Power Sources 195 (2010) 955–961.
[22] S. Nagata, A. Momma, T. Kato, Y. Kasuga, J. Power Sources 101 (2001) 60–71.
[23] D.L. Damm, A.G. Fedorov, J. Fuel Cell Sci. Technol. 2 (2005) 258–262.
[24] K.J. Daun, S.B. Beale, F. Liu, G.J. Smallwood, J. Power Sources 157 (1) (2006) 302–310.
[25] P. Aguiar, C.S. Adjiman, N.P. Brandon, J. Power Sources 138 (2004) 120–136.
[26] M. Iwata, T. Hikosaka, M. Morita, T. Iwanari, K. Ito, K. Onda, Y. Esaki, Y. Sakaki, S. Nagata, Solid State Ionics 132 (3–4) (2000) 297–308.
[27] Y. Zhao, C. Ou, J. Chen, Int. J. Hydrogen Energy 33 (15) (2008) 4161–4170.
[28] P.W. Li, L. Schaefer, M.K. Chyu, J. Heat Transfer Trans. ASME 126 (2) (2004) 219–229.
[29] J. Li, G.-Y. Cao, X.-J. Zhu, H.-Y. Tu, J. Power Sources 171 (2) (2007) 585–600.
[30] T. Tanaka, Y. Inui, A. Urata, T. Kanno, Energy Convers. Manage. 48 (5) (2007) 1491–1498.
[31] Y. Inui, N. Ito, T. Nakajima, A. Urata, Energy Convers. Manage. 47 (15–16) (2006) 2319–2328.
[32] Y. Inui, A. Urata, N. Ito, T. Nakajima, T. Tanaka, Energy Convers. Manage. 47 (13–14) (2006) 1738–1747.
[33] K. Fischer, J.R. Seume, J. Fuel Cell Sci. Technol. 6 (1) (2009).
[34] Z.J. Lin, J.W. Stevenson, M.A. Khaleel, J. Power Sources 117 (1–2) (2003) 92–97.